

Forward-Looking Geometric Configuration Optimization Design for Spaceborne-Airborne Multistatic Synthetic Aperture Radar

Deqing Mao ¹, Student Member, IEEE, Yongchao Zhang ¹, Member, IEEE, Jifang Pei ¹, Member, IEEE, Weibo Huo ¹, Member, IEEE, Yin Zhang ¹, Member, IEEE, Yulin Huang ¹, Senior Member, IEEE, and Jianyu Yang ¹, Member, IEEE

Abstract—Spaceborne-airborne multistatic synthetic aperture radar (SA-MuSAR) has the ability to provide high-resolution forward-looking imagery for receivers, but it relies on careful design of the geometric configuration (GC). In this article, a forward-looking GC optimization design method is proposed to obtain a high-quality fused image with limited observation time. First, the relationship between the spatial resolution and GC is illustrated by the wavenumber spectrum distribution of SA-MuSAR. Second, GC evaluators depending on the distribution of multiple wavenumber spectrum data are proposed. The GC design problem of coherent SA-MuSAR is transformed into a constrained multiobjective optimization problem. An intelligent evolutionary algorithm is adopted to optimize the wavenumber spectrum distribution. With the proposed method, high-quality forward-looking imagery can be obtained with a short observation time. Numerical simulations are carried out to verify the effectiveness of the proposed method.

Index Terms—Forward-looking geometric configuration (GC) design, spaceborne-airborne multistatic synthetic aperture radar (SA-MuSAR), wavenumber spectrum distribution.

I. INTRODUCTION

SPACEBORNE-AIRBORNE multistatic synthetic aperture radar (SA-MuSAR) system can provide forward-looking capability for receivers because it has the potential of flexible geometric configuration (GC) [1]–[4]. However, to obtain a high-quality fused image with limited observation time, the GC among the transmitter and receivers should be optimally designed, which essentially determines the quality of reconstructed images [5]–[7]. The ability to achieve high-quality imaging with a short observation time is significant for the survival of receivers in a confrontational working environment [8]. Fig. 1 shows the

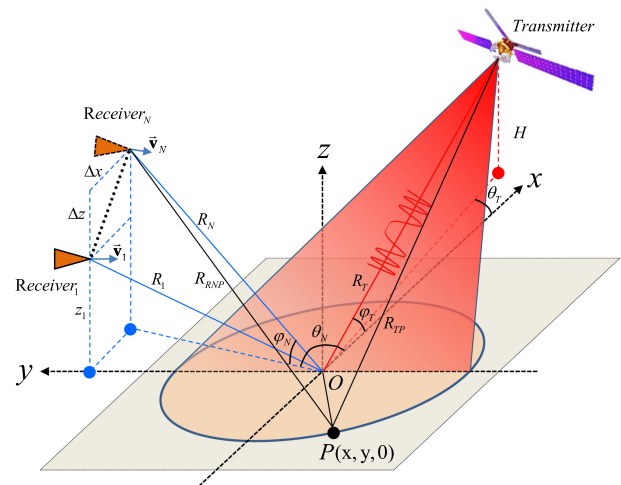


Fig. 1. Geometry model of an SA-MuSAR system.

geometry model of an SA-MuSAR system. The SA-MuSAR system consists of one transmitter and several receivers, and the receivers fly toward the target to provide a forward-looking imaging ability. In applications, the GC of SA-MuSAR is difficult to be fully defined. Especially, the effective range and the platform velocity highly depend on the practical platforms. In this article, we only design the relative GC spacings among the transmitter and the receivers, which is detailed in Section IV-A.

Many efforts have been done on designing the GC of SA-MuSAR for different desired missions [9]–[13]. The GC design methods can be divided into analytical methods [11]–[15] and optimization methods [9], [10]. The analytical methods can obtain the rules of the required indicators of different missions [16], [17]. In [17], a TechSat-21 system is proposed to achieve ground moving target indicator. In [18], to observe the height of targets by interferometric synthetic aperture radar, a GC named interferometric cartwheel is designed to achieve clutter rejection by coherently combining multiple measurements. Furthermore, to achieve quick revisit and wide-range coverage of the earth, a GC design method for spaceborne multistatic synthetic aperture radar (SAR) is proposed [19], [20]. However, the analytical methods cannot directly obtain an optimized result for the missions.

Manuscript received April 20, 2021; revised July 1, 2021 and July 27, 2021; accepted August 6, 2021. Date of publication August 10, 2021; date of current version August 26, 2021. This work was supported by the National Natural Science Foundation of China under Grants 61901092 and 61901090. (Corresponding author: Yongchao Zhang.)

Deqing Mao, Jifang Pei, Weibo Huo, Yin Zhang, Yulin Huang, and Jianyu Yang are with the School of Information and Communication Engineering, University of Electronic Science and Technology of China, Chengdu 611731, China (e-mail: mdq_uestc@163.com; peijfstudy@126.com; hwbuyi@163.com; yinzhang@uestc.edu.cn; yulinhuang@uestc.edu.cn; jyyang@uestc.edu.cn).

Yongchao Zhang is with the School of Information and Communication Engineering, University of Electronic Science and Technology of China, Chengdu 611731, China, and also with the Yangtze Delta Region, Quzhou 32400, China (e-mail: zhang_yongchao1@163.com).

Digital Object Identifier 10.1109/JSTARS.2021.3103802

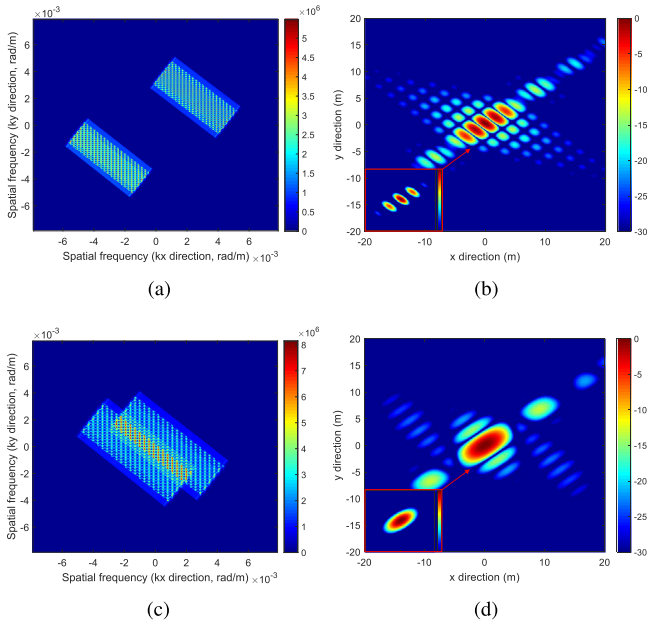


Fig. 2. Different WSR cases of SA-MuSAR. (a) Broken case. (b) PSF of broken case. (c) Overlapped case. (d) PSF of overlapped case.

In order to achieve the mission of obtaining a high-quality fused image with limited observation time, the GC of SA-MuSAR can be designed by optimization methods. The spatial resolution is one of the most important properties to be quantitatively evaluated in the design of the GC. The point spread functions (PSFs) of SA-MuSAR can be combined by coherent or incoherent fusion methods [10], [21]–[24]. In [25], the incoherent PSF of the global navigation satellite system-based multistatic SAR system is defined. In [21], the spatial resolution of the incoherent PSF is improved for sparse targets by the feature extraction method, but the incoherent spatial resolution cannot be essentially enhanced due to ignoring the phase relationship among the multiple stations [26], [27]. In [10] and [22], a GC optimization method is proposed by evaluating the characteristics of the incoherently fused PSF. The method can obtain an optimal GC for incoherent SA-MuSAR. However, the method cannot be extended to coherent SA-MuSAR because the -3 dB area size of the coherent PSF cannot be directly evaluated when it presents split mainlobe phenomenon [24], [28], [29]. As illustrated in Fig. 2(b) and [29], the split mainlobe phenomenon presents multiple high lobes. Many methods have been studied to suppress the split mainlobes [30]–[35]. In [33] and [34], a magnitude error and phase error estimation method is proposed to suppress the grating lobes in the range direction. In [31] and [32], a generalized range-Doppler-based azimuth reconstruction method is proposed to suppress the grating lobes in the cross-range direction. However, the repaired mainlobe based on these methods loses the unique mapping relationship between the PSF and the GC, which cannot be directly applied to evaluate the performance of the GC.

In this article, to obtain a high-quality fused image with limited observation time, a forward-looking GC optimization design method is proposed for coherent SA-MuSAR. The proposed

method evaluates the spatial resolution in the wavenumber domain because the spatial resolution of the coherent PSF cannot be truly evaluated when it presents split mainlobes. First, according to the forward-looking GC of SA-MuSAR, the wavenumber spectrum distribution is quantitatively deduced, which provides the relationship between the GC and imaging spatial resolution. Second, the quality of the GC is evaluated by establishing a set of GC estimators for the wavenumber spectrum distribution. The GC design problem can be transformed into a constrained multiobjective optimization problem (CMOP). Finally, an optimized forward-looking GC is obtained by solving the CMOP. Simulations are carried out to verify the proposed method.

The rest of this article is organized as follows. In Section II, the echo model of the SA-MuSAR system is introduced, and its wavenumber spectrum distribution is analyzed in detail. In Section III, the relationship between the spatial resolution and GC is analyzed. In Section IV, the GC evaluators for SA-MuSAR are designed by quantitatively optimizing the wavenumber spectrum distribution. Section V gives the simulations to verify the designed GC. Finally, Section VI concludes this article.

II. GC DESIGN MODELING FOR SA-MUSAR

A. Echo Model

As the geometry model in Fig. 1 shows, an SA-MuSAR system consists of one transmitter and N receivers. The transmitter is located at $(R_T, \theta_T, \varphi_T)$, where R_T denotes the range between the transmitter and the target O , θ_T is the azimuthal angle, and φ_T represents the pitch angle. Similarly, the N th receiver is located at $(R_N, \theta_N, \varphi_N)$. In Cartesian coordinates, the location can be expressed as $(x_N, y_N, z_N) = (R_N \cos \varphi_N \cos \theta_N, R_N \cos \varphi_N \sin \theta_N, R_N \sin \varphi_N)$. The receiver flies toward the target O with speed $\vec{v}_N = -\frac{\vec{a}}{|\vec{a}|} * v$, where $\vec{a} = (x_N, y_N, 0)$ and v denote the direction and the magnitude of speed, respectively. The initial positions of the receivers in the formation are evenly distributed between the first receiver and N th receiver, and the maximum spacing is $(\Delta x, 0, \Delta z)$. The target P is located on the ground plane at $(x, y, 0)$. The distances from the N th receiver and transmitter to the target P are R_{RNP} and R_{TP} , respectively.

The transmitter radiates a linear frequency modulation signal to obtain the target information. For the N th receiver, the signal received from the target P can be expressed as

$$S_N(\tau, t) = A \cdot \text{rect} \left(\frac{\tau}{T_a} \right) \cdot \text{rect} \left[\frac{t - R_{NP}(\tau)/c}{T_r} \right] \cdot \exp \left\{ -j \frac{2\pi f_c}{c} R_{NP}(\tau) + j\pi K_r [t - R_{NP}(\tau)/c]^2 \right\} \quad (1)$$

where A represents the echo amplitude, which is related to the target scattering coefficient and transmitted signal power. τ , t , T_a , and T_r denote the sampling slow time, sampling fast time, synthetic aperture time, and signal time width, respectively. The range history of the target P is $R_{NP}(\tau) = R_{TP}(\tau) + R_{RNP}(\tau)$. c represents the velocity of the electromagnetic wave. f_c and K_r denote the carrier frequency and the frequency chirp rate, respectively.

The echo data can be transformed into the range frequency domain using the principle of stationary phase [36] as

$$S_N(f_t, \tau) = A \cdot \text{rect}\left(\frac{\tau}{T_a}\right) \cdot \text{rect}\left(\frac{f_t}{K_r T_r}\right) \cdot \exp\left(-j\pi \frac{f_t^2}{K_r}\right) \cdot \exp\left[j\frac{2\pi}{c}(f_c + f_t)R_{\text{NP}}(\tau)\right] \quad (2)$$

where f_t represents the range frequency. According to coherent processing with the echo data of the reference target O , the echo data of point P can be represented as

$$S_N(f_t, \tau) = A \cdot \text{rect}\left(\frac{\tau}{T_a}\right) \cdot \text{rect}\left(\frac{f_t}{K_r T_r}\right) \cdot \exp\left\{j\frac{2\pi}{c}(f_c + f_t)[R_{\text{NP}}(\tau) - R_{\text{NO}}(\tau)]\right\} \quad (3)$$

where $R_{\text{NO}}(\tau) = R_T(\tau) + R_N(\tau)$ denotes the range history of the reference target. The range difference between the target P and the target O can be deduced as

$$\begin{aligned} & R_{\text{NP}}(\tau) - R_{\text{NO}}(\tau) \\ &= |R_{\text{TP}}(\tau) + R_{\text{RNP}}(\tau)| - |R_T(\tau) + R_N(\tau)| \\ &\approx x[\cos\varphi_T(\tau)\cos\theta_T(\tau) + \cos\varphi_N(\tau)\cos\theta_N(\tau)] \\ &+ y[\cos\varphi_T(\tau)\sin\theta_T(\tau) + \cos\varphi_N(\tau)\sin\theta_N(\tau)]. \end{aligned} \quad (4)$$

The transmitter and each receiver can form a spaceborne-airborne bistatic forward-looking SAR (SA-BiFSAR) structure. For the N th SA-BiFSAR pair, we can define the variables of the wavenumber spectrum in the x and y directions as

$$\begin{cases} k_{xN} = \frac{2\pi(f_c + f_t)}{c} [\cos\varphi_T(\tau)\cos\theta_T(\tau) + \cos\varphi_N(\tau)\cos\theta_N(\tau)] \\ k_{yN} = \frac{2\pi(f_c + f_t)}{c} [\cos\varphi_T(\tau)\sin\theta_T(\tau) + \cos\varphi_N(\tau)\sin\theta_N(\tau)]. \end{cases} \quad (5)$$

Therefore, the echo data in the wavenumber domain can be approximately expressed as

$$s_N(k_{xN}, k_{yN}) = A \cdot \exp[j(xk_{xN} + yk_{yN})]. \quad (6)$$

As (5) shows, the coordinates (k_{xN}, k_{yN}) in the wavenumber domain vary with the transmitted frequency and the spatial position of the stations. Therefore, the wavenumber spectrum distribution, also called the wavenumber-domain support region (WSR), of the N th bistatic pair can be obtained by coordinate projection of the echo data, which provides the relationship between the spatial resolution and GC. The WSR can reflect the spatial resolutions in different directions by analyzing its spatial bandwidths [9], [37], [38]. For the N th bistatic pair, the range of the WSR can be expressed as

$$\begin{cases} \mathbf{k}_{xN}(\tau, f_t) \in [k_{x\min N}, k_{x\max N}] \\ \mathbf{k}_{yN}(\tau, f_t) \in [k_{y\min N}, k_{y\max N}] \end{cases} \quad (7)$$

where $\mathbf{k}_{xN}(\tau, f_t)$ and $\mathbf{k}_{yN}(\tau, f_t)$ represent the vectors of the wavenumber spectrum variables in the x and y directions of the N th bistatic pair, respectively. $[k_{x\min N}, k_{x\max N}]$ and $[k_{y\min N}, k_{y\max N}]$ define the analyzed range boundaries of the

WSR in the x and y directions of the N th bistatic pair, respectively.

B. PSF of Coherent SA-MuSAR

The SA-MuSAR system shown in Fig. 1 consists of N bistatic pairs. The wavenumber spectrum distribution of the SA-MuSAR system can be formed by several individual WSRs. However, because the spatial locations of the receivers are distributed, the positions of the WSRs are determined by the relative spatial sampling relationship. We can define the analyzed range boundaries of WSRs with respect to the x and y directions as

$$\begin{cases} k_{x\min} = \min\{k_{x\min 1}, \dots, k_{x\min N}\} \\ k_{y\min} = \min\{k_{y\min 1}, \dots, k_{y\min N}\} \\ k_{x\max} = \max\{k_{x\max 1}, \dots, k_{x\max N}\} \\ k_{y\max} = \max\{k_{y\max 1}, \dots, k_{y\max N}\} \end{cases} \quad (8)$$

where $\min\{\cdot\}$ and $\max\{\cdot\}$ denote minimum and maximum value operations, respectively. Based on the position relationship among the multiple stations, the echo data can be projected into a new coordinate range. The echo data of the SA-MuSAR system can be projected into the wavenumber domain together as

$$s(k_x, k_y) = \sum_{n=1}^N A'_n s_n(k_{xn}, k_{yn}) \quad (9)$$

where A'_n denotes the normalized amplitude of the fused wavenumber spectrum.

To analyze the spatial resolution of the SA-MuSAR system, the relationship between the wavenumber spectrum and the PSF can be expressed by matrix Fourier transform (MFT) [23] as

$$\sigma(x, y) = \iint_{(k_x, k_y) \in \Omega} s(k_x, k_y) e^{-(jxk_x + jyky)} dk_x dk_y \quad (10)$$

where $\sigma(x, y)$ denotes the target scattering coefficient at the (x, y) position. Ω represents the effective range defined by the boundaries of WSRs of the SA-MuSAR system

C. GC Design Modeling for Incoherent Multistatic SAR

The incoherent multistatic SAR ignores the relative phase differences between the multiple bistatic pairs [25], [26]. The incoherent PSF of multistatic SAR is focused, and its quality can be directly evaluated in the spatial domain by different characteristics, such as the -3 dB area size and the resolution equilibrium degree [10], [38]–[41]. The GC design problem of incoherent multistatic SAR can be modeled as a constrained optimization problem by several GC evaluators as [10]

$$\begin{cases} \min \rho(\vec{\mathbf{g}}) & \text{(i)} \\ \min \eta(\vec{\mathbf{g}}) = \frac{\rho_{\theta_{\max}}(\vec{\mathbf{g}})}{\rho_{\theta_{\min}}(\vec{\mathbf{g}})} & \text{(ii)} \\ \text{s.t. } \vec{\mathbf{g}} \in \Omega_1 \end{cases} \quad (11)$$

where $\vec{\mathbf{g}}$ denotes the GC vector that describes the relative locations of the transmitter and receivers. Ω_1 represents the vector space of $\vec{\mathbf{g}}$. The evaluators in (i) and (ii) represent different requirements for the spatial resolution of SAR, and they penalize different characteristics of the PSF to acquire high-quality radar imagery. In evaluator (i), the area size of the

spatial resolution ρ varies with the GC vector. Evaluator (i) aims to obtain a high spatial resolution with small -3 dB area size. In evaluator (ii), the spatial resolution equilibrium coefficient η varies with the spatial resolutions in the maximum and minimum resolution directions. Evaluator (ii) aims to obtain a balanced spatial resolution by optimizing the shape of the -3 dB area. However, the PSF of coherent multistatic SAR may present a split mainlobe phenomenon when an inappropriate GC makes the wavenumber spectrum distribution noncontinuous [24]. The traditional analysis method in the spatial domain cannot reflect the real spatial resolution of coherent multistatic SAR, which results in the requirements in (11) being difficult to optimize.

III. SPATIAL RESOLUTION ANALYSIS OF COHERENT SA-MUSAR

To design an optimized GC, the relationship between the spatial resolution and the GC for the coherent SA-MuSAR system can be clearly illustrated in the wavenumber domain.

A. Imaging Profile Analysis in an Arbitrary Direction

The imaging profiles of the PSF can be applied to analyze the resolutions in different directions. In (10), the PSF is reconstructed by the MFT method. In another way, the imaging profile in an arbitrary direction can be conveniently obtained by utilizing the two-dimensional (2-D) projection slice theorem [42]. The imaging profile in the ϕ_i direction can be represented by the Fourier transform of the projected slice of the wavenumber spectrum data. The projected slice can be expressed as

$$\begin{aligned} \rho_f(k_r, \phi)|_{\phi=\phi_i} &= \\ \iint_{(k_x, k_y) \in \Omega} s(k_x, k_y) \delta(k_r - k_x \cos \phi_i - k_y \sin \phi_i) dk_x dk_y & \quad (12) \\ \rho_f(k_r, \phi)|_{\phi=\phi_i} &= \sum_{n=1}^N \iint_{(k_{xn}, k_{yn}) \in \Omega} s_n(k_{xn}, k_{yn}) \delta(k_r \\ - k_{xn} \cos \phi_i - k_{yn} \sin \phi_i) dk_{xn} dk_{yn} & \\ = \sum_{n=1}^N \rho_f \left(\frac{k_r - k_{cn}}{B_{kn}}, \phi_i \right). & \quad (13) \end{aligned}$$

where $\delta(\cdot)$ denotes the delta function. (k_r, ϕ) represents the polar coordinates of the projected wavenumber spectrum. Based on the relationship between multiple stations, the projected wavenumber spectrum slice can be transformed into (13), where B_{kn} and k_{cn} denote the bandwidth and center frequency of the n th projected wavenumber spectrum, respectively.

The imaging profile in the ϕ_i direction can be obtained by

$$\begin{aligned} \sigma(r, \phi)|_{\phi=\phi_i} &= \int_{k_r \in K} \rho_f(k_r, \phi)|_{\phi=\phi_i} e^{-j2\pi r k_r} dk_r \\ &= \sum_{n=1}^N \int_{k_r \in K} \rho_f \left(\frac{k_r - k_{cn}}{B_{kn}}, \phi_i \right) e^{-j2\pi r k_r} dk_r & \quad (14) \end{aligned}$$

where r represents the relative distance with respect to the reference target, and K denotes the range of k_r .

Specifically, an SA-MuSAR system consisting of two receivers is taken as an example to analyze the spatial resolution in detail. The imaging profile in (14) can be rewritten as

$$\begin{aligned} \sigma'(r, \phi)|_{\phi=\phi_i} &= \\ \int_{k_r \in K} \left[\rho_f \left(\frac{k_r - k_{c1}}{B_{k1}}, \phi_i \right) + \rho_f \left(\frac{k_r - k_{c2}}{B_{k2}}, \phi_i \right) \right] e^{-j2\pi r k_r} dk_r. & \quad (15) \end{aligned}$$

Based on the different GCs, the bandwidth and center frequency of the projected wavenumber spectrum can present different characteristics.

1) *Imaging Profile of Discontinuously Sampled Data:* In (15), when the echo slice of the projected wavenumber spectrum is discontinuously sampled, the relationship between the bandwidth and center frequency of the projected wavenumber spectrum can be expressed as

$$|k_{c1} - k_{c2}| > (B_{k1} + B_{k2})/2 \quad (16)$$

where the meaning of the subscripts will not be repeated. The gap band can be expressed as

$$B_g = |k_{1c} - k_{2c}| - |B_{k1} + B_{k2}|/2. \quad (17)$$

The recovered profile can be obtained by the fast Fourier transform operation as

$$\begin{aligned} \sigma'(r - r_c) &= \delta(r - r_c) \otimes \\ \left[B_{k1} A_1(r) \text{sinc}(B_{k1} r) \cdot \exp(j2\pi k_{c1} r) \right] & \quad (18) \\ + B_{k2} A_2(r) \text{sinc}(B_{k2} r) \cdot \exp(j2\pi k_{c2} r) & \end{aligned}$$

where r_c represents the center distance to the reference target. \otimes denotes the convolution operation. The bandwidth–amplitude products of the recovered profiles are simplified as $B_{k1} A_1(r) \text{sinc}(\cdot)$ and $B_{k2} A_2(r) \text{sinc}(\cdot)$.

From the coherent imaging profile in (18), it is seen that the recovered profile is determined by the signal with the larger bandwidth–amplitude product when the bandwidth and amplitude are different. When the bandwidth–amplitude products are similar, the imaging result is mainly determined by the phase information. The coherent imaging profile can be transformed into

$$\begin{aligned} \sigma'(r - r_c) &= \delta(r - r_c) \otimes \\ \{BA(r) \text{sinc}(Br) [1 + \exp(j2\pi \Delta k_c r)] \exp(j2\pi k_{c1} r)\} & \quad (19) \end{aligned}$$

where $B = B_{k1} = B_{k2}$, $A(r) = A_1(r) = A_2(r)$, and $\Delta k_c = k_{c2} - k_{c1}$. The phase difference is determined by the projected data gap. In (19), the bandwidth B determines the -3 dB width of the amplitude envelope, and $r_{-3} = 0.886/B$ [43]. The -3 dB mainlobe appears to split when the phase difference Δk_c is larger than $B/0.886$. As the phase difference in (19) increases, the splitting of the PSF mainlobe becomes serious.

2) *Imaging Profile of Continuously Sampled Data:* In (15), when the echo slice is continuously sampled, the projected

wavenumber spectrum can be described by

$$|k_{c1} - k_{c2}| \leq (B_{k1} + B_{k2}) / 2. \quad (20)$$

The reconstructed profile can be expressed as

$$\begin{aligned} \sigma'(r - r_c) &= \delta(r - r_c) \otimes \\ &[B_{k_o} A_o(r) \text{sinc}(B_{k_o} r) \exp(j2\pi k_{c_o} r)] \end{aligned} \quad (21)$$

where B_{k_o} , $A_o(r)$, and k_{c_o} denote the bandwidth, amplitude, and center frequency of the projected continuous wavenumber spectrum, respectively. The continuous wavenumber spectrum slice can avoid the split mainlobe problem. According to (19) and (21), the projected wavenumber slices can explain the reason for the split mainlobe phenomenon. The GC design problem of SA-MuSAR can be converted into the wavenumber domain for easy evaluation.

B. WSR of Coherent SA-MuSAR

Based on the deduction of the imaging profile above, it is seen that the wavenumber spectrum of SA-MuSAR is different from that of the SA-BiFSAR system, which may not be continuous in some cases because the GC of the multiple receivers is complex. For example, an SA-MuSAR system consists of two receivers, and the common cases of its wavenumber spectrum distribution can be divided into broken and overlapped cases, as shown in Fig. 2.

In Fig. 2(a), when the receivers are spatially distributed, the wavenumber spectrum distribution is broken. The projected slices of the broken case must be sampled with a data gap in some directions. Based on the analysis of the imaging profiles, the broken WSR is the essential reason for the split mainlobe phenomenon, as the reconstructed PSF shown in Fig. 2(b). In Fig. 2(c), the wavenumber spectrum distribution of the SA-MuSAR is overlapped because the viewing angles of multiple receivers are covered. In Fig. 2(d), the reconstructed PSF of the overlapped case is focused.

The different distributions of the wavenumber spectrum can directly illustrate the spatial sampling ability of the SA-MuSAR system, which forms the relationship between the spatial resolution and the system GC [24]. For the broken wavenumber spectrum, the projected slices in some directions are sampled with gaps, which results in the undesirable split mainlobe. The traditional -3 dB area size of the PSF [10] cannot reflect the real spatial resolution performance of coherent SA-MuSAR. For the overlapped wavenumber spectrum, the projected slices are continuous, which can obtain a focused PSF. The wavenumber spectrum distribution can straightforwardly reflect the performance of the GC.

C. Enclosing Shape of the WSR

In addition to the relative position of the wavenumber spectrum, the shape of the WSR should be constrained, which determines the angle between the range and cross-range resolutions. The angle should be nonparallel to obtain 2-D high-resolution radar imagery. Based on the principle of the 2-D Fourier transform, the angle between the range and cross-range resolutions is related to the enclosing shape of the WSR.

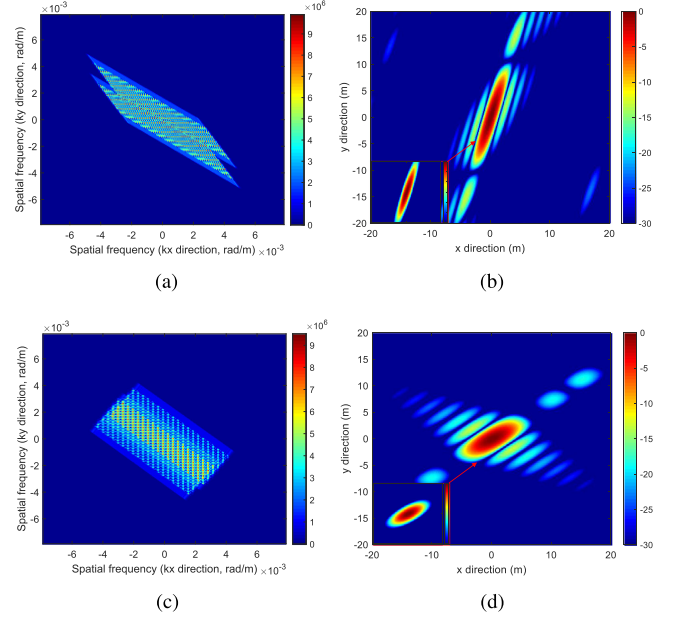


Fig. 3. Relationship between the wavenumber spectrum and PSF. (a) WSR1. (b) PSF of WSR1. (c) WSR2. (d) PSF of WSR2.

As shown in Fig. 3, the PSFs present different characteristics depending on the WSR shape. In Fig. 3(a), the enclosing shape of the WSR presents a parallelogram. The reconstructed target in Fig. 3(b) presents a skewed PSF. In Fig. 3(c), the enclosing shape of the WSR is a rectangle. The reconstructed target presents a regular PSF, as shown in Fig. 3(d). The inclination direction of the enclosing shape determines the resolution angle of the PSF. For the SA-MuSAR system, a regular shape of the fused WSR is preferred.

As in the analysis above, the relative GC of coherent SA-MuSAR can be evaluated by the distribution of the wavenumber spectrum. The spatial resolution characteristics of the coherent SA-MuSAR, such as the spatial resolution size, resolution equilibrium degree, and shape of the PSF, can be easily evaluated in the wavenumber domain. The size of the spatial resolution can be evaluated by that of the wavenumber spectrum distribution. The imaging profiles can be applied to evaluate the resolution equilibrium degree in different directions. The enclosing shape of WSRs can be used to assess the resolution angle.

IV. GC EVALUATORS AND OPTIMIZATION DESIGN FOR SA-MUSAR

To evaluate the spatial resolution of coherent SA-MuSAR in the wavenumber domain, several GC evaluators are proposed by assessing the characteristics of the wavenumber spectrum distribution. The evaluators can transform the forward-looking GC design problem into a CMOP. The optimized forward-looking GC can be obtained by solving the CMOP.

A. Designed Forward-Looking GC Vector for SA-MuSAR

In the SA-MuSAR system, receiver 1 serves as a leader platform. The parameters related to the forward-looking GC of the SA-MuSAR system are various. We take the leading receiver

TABLE I
MAIN SYSTEM PARAMETERS

System parameters		GC parameters	
Carrier frequency	9.6 GHz	Location of transmitter	(514, 0, 100) km
Bandwidth	120 MHz	Location of leading receiver	$\mathbf{r}_1 = (x_1, y_1, z_1)$ $= (R \cos\theta_1, R \sin\theta_1, H_1)$
Sampling frequency	180 MHz	Location of the following receiver	$\mathbf{r}_2 = (x_1, y_1, z_1) + (\Delta x, 0, \Delta z)$
Time width	10 μ s	Pulse repetition frequency	800 Hz
Range of the leading receiver	20 km	Magnitude of receiver speed	340 m/s
Designed GC parameters			
Synthetic aperture time		$T_a \in [0.5s, 3s]$	
Azimuthal angle		$\Delta\theta \in [5^\circ, 175^\circ]$	
Formation spacing		$\Delta x \in [0 \text{ m}, 500 \text{ m}], \Delta z \in [0 \text{ m}, 1000 \text{ m}]$	

as an example. The range between the target and receiver R_1 and the velocity of the receivers \vec{v}_1 have different influences on the imaging result. However, these parameters are not deeply considered in this article because they are usually limited by the ability of practical airborne platforms. The target range and the velocity of receivers are directly chosen according to the mission.

In addition, the viewing angle between the transmitter and leading receiver $\Delta\theta = \theta_1 - \theta_T$, and the formation spacing $(\Delta x, \Delta z)$ are optimally designed in this article. For an SA-MuSAR system, the forward-looking GC vector \vec{g} can be specifically expressed as

$$\vec{g} = (\vec{I}, T_a)^T = (\Delta\theta, \Delta x, \Delta z, T_a)^T \quad (22)$$

where \vec{I} denotes the location vector of the SA-MuSAR system, which describes the relative spatial relationship between the transmitter and receivers. The forward-looking GC vector is directly related to the imaging quality. Based on the relationship between the spatial resolution and the GC vector, the optimized GC of SA-MuSAR can be obtained by solving the CMOP. However, the evaluators in (11) are not applicable in the SA-MuSAR system because the characteristics of the coherently fused PSF are different from those of the incoherently fused PSF. The simulated parameters of an SA-MuSAR system consisting of two receivers are shown in Table I.

B. GC Evaluators for the Wavenumber Spectrum Distribution

To obtain the optimized GC of SA-MuSAR, the GC evaluators in (11) can be transformed into those in the wavenumber domain as

$$\begin{cases} \min \rho_g(\vec{g}) & (a) \\ \min \eta(\vec{g}) & (b) \\ \min \theta(\vec{g}) = |\Delta\theta(\vec{g}) - 90^\circ| & (c) \\ \min S'(\vec{g}) = \max\{S_{(1,2)}(\vec{g}), \dots, S_{(N-1,N)}(\vec{g})\} & (d) \end{cases} \quad (23)$$

s.t. $\begin{cases} S_{o \min}(\vec{g}) = \min\{S_{(1,2)}(\vec{g}), \dots, S_{(N-1,N)}(\vec{g})\} > 0 \\ \vec{g} = (\Delta\theta, \Delta x, \Delta z, T_a) \in \Omega_2 \end{cases}$

where Ω_2 represents the decision space of vector \vec{g} given in Table I. Evaluators (a) and (b) denote the optimizations for the spatial resolution size and the resolution equilibrium

degree, respectively. Evaluator (c) constrains the degree of regulation of the PSF. $\Delta\theta(\vec{g})$ is the angle between the range and cross-range resolutions. Evaluator (d) represents minimization of the overlapped area size between each wavenumber spectrum, which constrains the echo acquisition efficiency. $S_{(N-1,N)}(\vec{g})$ denotes the overlapped area size of the $(N-1)$ th and N th receivers. However, $S_{o \min}(\vec{g})$ means that the minimum overlapped area of the wavenumber spectrum should exist, which constrains the continuity of the wavenumber spectrum. The proposed evaluators form a CMOP to penalize different characteristics of the PSF to acquire high-quality radar imagery with a short observation time.

1) *Evaluation of the Spatial Resolution Size*: From (10), it is seen that the relationship between the PSF and the wavenumber spectrum can be expressed by the 2-D Fourier transform. The spatial resolution size is inversely proportional to the area size of the wavenumber spectrum. Even if the -3 dB area size of the PSF cannot be calculated, the inverse relationship between the spatial resolution size and the wavenumber spectrum distribution still holds.

To evaluate the size of spatial resolution of SA-MuSAR, we define the generalized spatial resolution in the wavenumber domain as

$$\rho_g(\vec{g}) = \frac{1}{S_w(\vec{g})} \quad (24)$$

where S_w denotes the area size of the WSR. The generalized spatial resolution is not equal to the -3 dB area size of the PSF, but a linear relationship can be formed between them.

When the synthetic aperture time is fixed at 2 s, the relationship between the generalized spatial resolution and the location vector is given in Fig. 4. The height of the leading receiver H_1 is 10 km. The range of the leading receiver R is 20 km. As shown in Fig. 4(a), for different horizontal spacings, the generalized spatial resolution varies with the azimuthal angle between the transmitter and the leading receiver. When the angle is close to zero, the spatial resolution becomes poor. As shown in Fig. 4(b), the height spacing has a similar influence on the generalized spatial resolution with that of the horizontal spacing. However, their optimal solutions are different. If traditional solution methods are adopted [44], [45], the optimized solution may not exist.

2) *Spatial Resolution Equilibrium Coefficient*: For understandable radar imagery, the spatial resolutions of the PSF in different directions should be balanced. To evaluate the equilibrium property of the PSF, the resolution equilibrium degree in (11)-ii can be evaluated by the equilibrium coefficient in the wavenumber domain as

$$\eta(\vec{g}) = \frac{B_k(\vec{g}, \phi_{\max})}{B_k(\vec{g}, \phi_{\min})} \quad (25)$$

where $B_k(\vec{g}, \phi_{\max})$ and $B_k(\vec{g}, \phi_{\min})$ represent the projected bandwidth of the wavenumber spectrum in the maximum resolution direction ϕ_{\max} and the minimum resolution direction ϕ_{\min} , respectively.

As shown in Fig. 5, the spatial resolution equilibrium coefficient varies with the formation spacing and the azimuthal angle. However, the rules of the equilibrium degree are different from

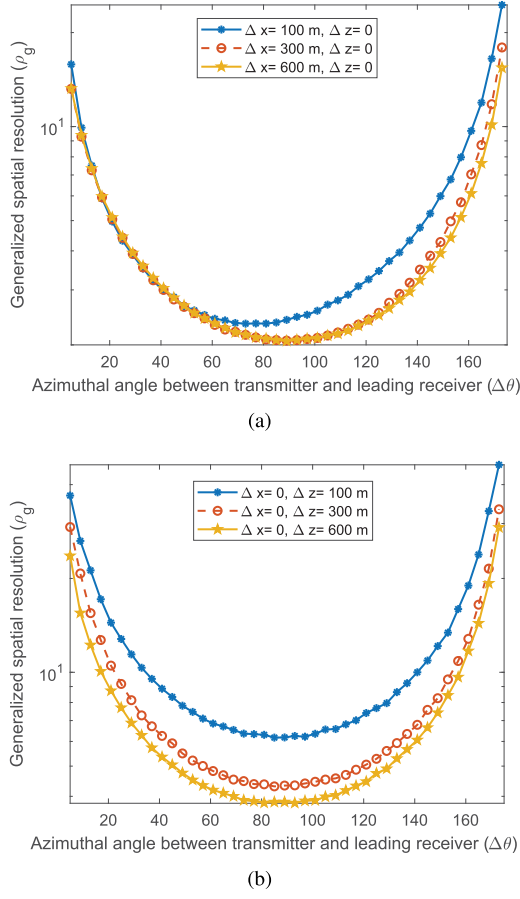


Fig. 4. Generalized spatial resolution with respect to $\Delta\theta$. (a) Different horizontal spacings. (b) Different height spacings.

those of the spatial resolution. In Fig. 5(a), for different spacings, the equilibrium coefficient is nonconvex along the azimuthal angle. In Fig. 5(b), the height spacings and the azimuthal angle jointly determine the equilibrium coefficient.

3) *Evaluation of the Shape of the WSR*: To obtain a regular PSF, the angle condition in (23) is difficult to be achieved because the ideal orthogonal angle is not conducive to other evaluation indicators. Because the angle between the range and cross-range resolutions can be reflected in the wavenumber domain [46], we can approximately evaluate the shape of the WSR. The fill factor of the WSR can be defined as

$$\xi(\vec{g}) = \frac{S_w(\vec{g})}{S_r} \quad (26)$$

where S_r represents the area size of the enclosing rectangle of the WSR.

The area size of the enclosing rectangle of the WSR can be conveniently obtained from the projected slices as

$$S_r(\phi_i) = B_{\rho_f(\phi_i)} \cdot B_{\rho_f(\phi_i + \pi/2)} \quad (27)$$

where $B_{\rho_f(\phi_i)}$ and $B_{\rho_f(\phi_i + \pi/2)}$ denote the projected bandwidth of the wavenumber spectrum in the ϕ_i direction and its orthogonal direction, respectively. The minimum area size of the enclosing rectangles can be expressed as

$$S_{r \min} = \min \{S_r(\phi_1), \dots, S_r(\phi_i), \dots, S_r(\phi_I)\} \quad (28)$$

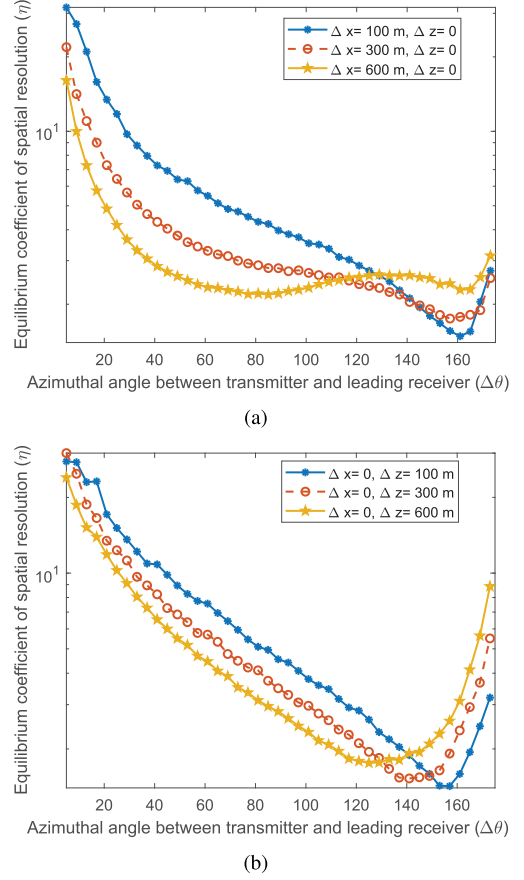


Fig. 5. Spatial resolution equilibrium coefficient with respect to $\Delta\theta$. (a) Different horizontal spacings. (b) Different height spacings.

where I denotes the number of projected slices obtained by the PST. Therefore, the maximum fill factor of the WSR can be expressed as

$$\xi_{\max}(\vec{g}) = \frac{S_w(\vec{g})}{S_{r \min}}. \quad (29)$$

Based on the optimization of the fill factor of the WSR, a regular shape of the fused WSR can be obtained. In Fig. 6, the fill factor varies with the azimuthal angle $\Delta\theta$. In Fig. 6(a), the fill factor decreases as the horizontal spacings increase. Comparing Fig. 6(a) and (b), the influences of the horizontal spacing and height spacing on the fill factor are different. The fill factor function is not a convex function, which makes obtaining an optimal solution difficult. Based on the defined fill factor, the GC evaluator in (23) can be transformed as

$$\min \xi'(\vec{g}) = 1 - \xi_{\max}(\vec{g}). \quad (30)$$

4) *Echo Acquisition Efficiency of SA-MuSAR*: In addition to the location vector, the synthetic aperture time has a significant influence on the imaging quality. When the overlapped area size of the multiple wavenumber spectrum is large, the observed information of the targets is redundant. The overlapped area size of the observed wavenumber spectrum can be expressed as

$$S_{(N-1, N)}(\vec{g}) = S_{w_{N-1}}(\vec{g}) \cap S_{w_N}(\vec{g}) \quad (31)$$

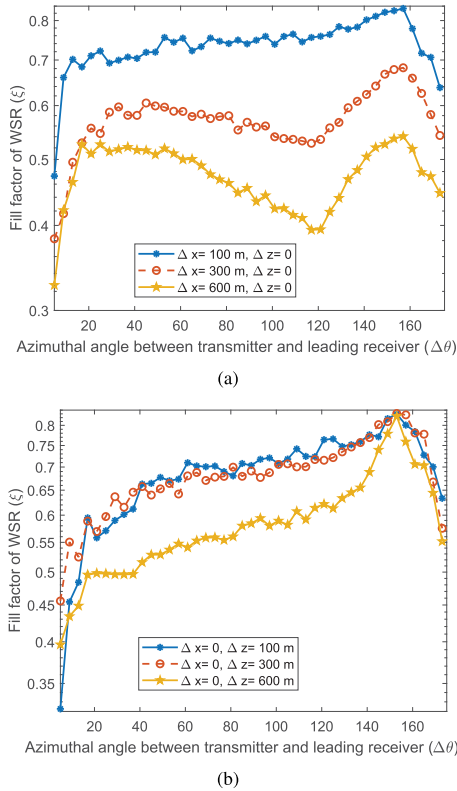


Fig. 6. Fill factor of WSR with respect to $\Delta\theta$. (a) Different horizontal spacings. (b) Different height spacings.

where $S_{wN-1}(\vec{g})$ and $S_{wN}(\vec{g})$ represent the area size of the wavenumber spectrum of the $(N-1)$ th receiver and N th receiver, respectively. In applications, we aim to observe more information with a shorter observation time. The echo acquisition efficiency coefficient can be defined as

$$\mu(\vec{g}) = 1 - \frac{\sum_{n=1}^{N-1} S_{(n,n+1)}(\vec{g})}{S_{r \min}}. \quad (32)$$

The GC evaluator in (23) can be normally transformed into the evaluation of the echo acquisition efficiency coefficient as

$$\min \mu'(\vec{g}) = 1 - \mu(\vec{g}). \quad (33)$$

According to the minimization of the overlapped area size, the echo acquisition efficiency can be improved.

C. GC Optimization Design Solution

To obtain the optimized GC of SA-MuSAR, the GC evaluators in (23) can be transformed into

$$\begin{cases} \min \rho_g(\vec{g}) = \frac{1}{S_w(\vec{g})} \\ \min \eta(\vec{g}) = \frac{B_k(\vec{g}, \phi_{\max})}{B_k(\vec{g}, \phi_{\min})} \\ \min \xi'(\vec{g}) = 1 - \xi_{\max}(\vec{g}) \\ \min \mu'(\vec{g}) = 1 - \mu(\vec{g}) \end{cases} \quad (34)$$

$$\text{s.t. } \begin{cases} S_{o \min}(\vec{g}) > 0 \\ \vec{g} = (\Delta\theta, \Delta x, \Delta z, T_a) \in \Omega_2. \end{cases}$$

The proposed GC evaluators form a CMOP to penalize different characteristics of the wavenumber spectrum to acquire high-quality radar imagery with a short observation time. However, based on the analysis above, traditional convex optimization methods are not applicable to the multiple objectives problem. To solve the CMOP, the nonlinear constrained nondominated sorting genetic algorithm II (NC-NSGA II) is adopted in this article [47], [48]. NC-NSGA II is a fast and effective intelligent evolutionary algorithm. The main steps of the algorithm can be carried out as follows.

1) *Initialization of the GC Optimization Design Problem:* The initialization of the GC optimization design problem consists of two parts. First, the parameters of the SA-MuSAR system are set. Second, the intelligent evolutionary algorithm is initialized, such as the number of maximum generations G_{\max} , population size K_P , proportion of optimal solution P_γ , crossover proportion P_c , and mutation proportion P_m . The initial population $\mathbf{I}^0 = \{\vec{g}_1, \dots, \vec{g}_{K_P}\}$ of the GC vector is randomly generated from the decision space. The values of the objective functions are calculated according to (34). The parameters P_c , P_m , and P_γ are basic initial parameters of the genetic algorithm [47], [49]. P_c and P_m determine the crossover population and mutation population proportions in the optimization algorithm, respectively. They influence the operational time of the algorithm. The proportion P_γ and population size K_P determine the number of output solutions $P_\gamma * K_P$.

2) *Crossover and Mutation Operation:* For the G th generation, the population \mathbf{I}^G is used to generate the offspring population \mathbf{O}^G relying on the crossover operator and mutation operator [50]. The generated offspring population \mathbf{O}^G and parent population \mathbf{I}^G are combined to obtain the population $\mathbf{P}^G = \mathbf{O}^G \cup \mathbf{I}^G$.

3) *Nondominated Sorting:* Based on the constraint in (34), the solutions may be either feasible or infeasible. The concept of constrained domination is introduced into the nondominated sorting. A solution \mathbf{P}_i^G is said to constrained-dominate a solution \mathbf{P}_j^G ($\mathbf{P}_i^G \prec_c \mathbf{P}_j^G$), if any of the following conditions is true [47]: a) solution \mathbf{P}_i^G is feasible and solution \mathbf{P}_j^G is not; b) solutions \mathbf{P}_i^G and \mathbf{P}_j^G are both infeasible, but solution \mathbf{P}_i^G has a smaller constraint value; or c) solutions \mathbf{P}_i^G and \mathbf{P}_j^G are feasible and solution \mathbf{P}_i^G dominates solution \mathbf{P}_j^G . Using this constrained-domination principle, any feasible solution can have a better nondomination rank than any infeasible solution. All feasible solutions are ranked according to their objective function values and constraint values. The solutions with the same nondomination level are assigned to the same nondominated front.

4) *Tournament Selection:* The crowding distances of the solutions for each nondominated front are calculated to evaluate its crowding degree. The Binary tournament selection based on the crowding comparison operator and rank is utilized to choose the generated population \mathbf{U}^{G+1} [51]. The generated population \mathbf{U}^{G+1} is then assigned for crossover and mutation to create the new parent population \mathbf{I}^{G+1} . The tournament size is $T = P_\gamma * K_P$.

5) *Selection of the Optimized GC:* Based on the evolutionary update process in steps 2) to 4), multiple optimal solutions of GC vectors can be obtained when the number of iterative generations

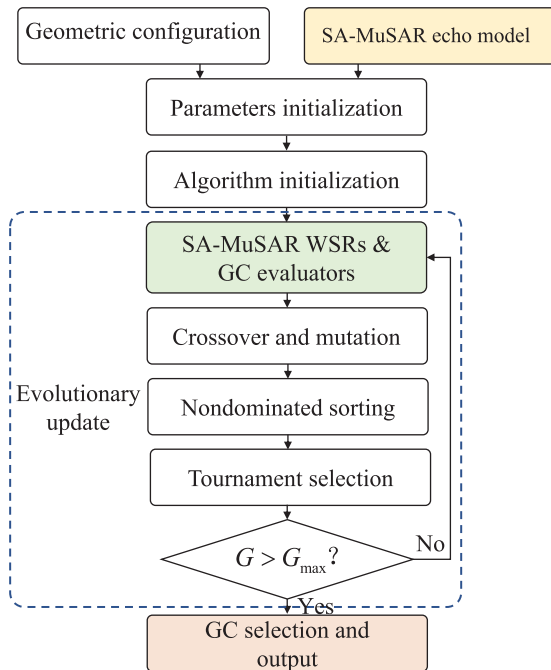


Fig. 7. Flowchart of the proposed GC optimization design method.

is greater than G_{\max} . However, the PSFs of the solutions may present different characteristics. To evaluate the performance of the designed GC, the peak-to-sidelobe ratio (PSLR) and integrated sidelobe ratio (ISLR) in different directions of the reconstructed PSF are compared.

Based on the above analysis, the flowchart of the proposed GC optimization design method is shown in Fig. 7.

V. SIMULATIONS AND PERFORMANCE VERIFICATION

A. Solutions of the Optimized GC

The parameters of an SA-MuSAR system are given in Table I. The height of the leading receiver is $H_1 = 10$ km. The parameters of the NC-NSGA II method are set as follows, the number of maximum generations $G_{\max} = 200$, population size $K_P = 30$, proportion of optimal solution $P_\gamma = 0.1$, crossover proportion $P_c = 0.8$, and mutation proportion $P_m = 0.2$. Based on the iterative evolutionary update, the solutions of the CMOP are shown in Table II.

As seen in the top part of Table II, the designed parameters can provide three feasible GCs for the SA-MuSAR system. The designed GCs can provide different flight directions for the receivers. In the bottom part, the performance in terms of the optimized spatial resolution of the corresponding GC is given. The spatial resolutions of the designed GCs present different characteristics. The first GC can obtain a balanced PSF. The second GC provides the most regular PSF. The third GC has the highest spatial resolution. The target information acquisition efficiency of all designed GCs can be greater than 90%.

B. Spatial Resolution Verification

1) *PSF Verification*: Based on the optimized GC solutions, the point target is simulated to verify their effectiveness. The

TABLE II
GC SOLUTIONS OF THE CMOP AND THE SPATIAL RESOLUTION PERFORMANCE

Number	Designed parameters			
	$\Delta\theta$ (degree)	Δx (m)	Δz (m)	T_a (s)
GC 1	115.67	37.75	371.37	2.30
GC 2	114.86	32.14	370.29	2.25
GC 3	109.81	34.05	370.18	2.29
Number	Performance of PSFs			
	ρ_g (m ²)	η	ξ	μ
GC 1	3.80	1.96	77.66%	90.08%
GC 2	3.86	2.07	80.21%	90.09%
GC 3	3.63	2.19	77.11%	90.05%

TABLE III
PSLRs AND ISLRs OF THE FUSED PSFs

Mainlobe and sidelobe performance			
GC No. / Indexes	GC 1	GC 2	GC 3
PSLR(ϕ_{\max})	-20.61 dB	-20.89 dB	-20.76 dB
PSLR(ϕ_{\min})	-30.25 dB	-30.89 dB	-31.35 dB
PSLR(ϕ_{range})	-13.82 dB	-13.82 dB	-13.83 dB
PSLR(ϕ_{cross})	-11.60 dB	-11.62 dB	-11.62 dB
ISLR(ϕ_{\max})	-9.51 dB	-9.66 dB	-9.64 dB
ISLR(ϕ_{\min})	-14.93 dB	-14.92 dB	-15.36 dB
ISLR(ϕ_{range})	-10.18 dB	-10.16 dB	-11.13 dB
ISLR(ϕ_{cross})	-9.36 dB	-9.31 dB	-9.58 dB

imaging results based on the designed GCs and each bistatic pair are shown in Fig. 8.

In Fig. 8(a)–(c), the WSRs of the designed GCs are shown. The designed WSRs are continuous based on the different GC vectors. In Fig. 8(d)–(f), the PSFs of the leading receiver of different GCs are given. Fig. 8(g)–(i) show the results of the following receiver. The imaging results based on a single receiver are limited. Based on the designed GCs of the receivers, the fused imaging results present high spatial resolution. The fused PSFs based on the designed GCs are balanced, focused, and regular. Based on a quantitative comparison of the imaging results, the -3 dB area size of the fused PSF can be improved by nearly twofold. The spatial resolution of the fused PSF is balanced, and its equilibrium coefficient can be closer to 1. With the same observation time, the proposed SA-MuSAR system presents better imaging quality than the SA-BiFSAR system. In addition, the performance of the feasible solutions is much better than that of the inappropriate GCs shown in Figs. 2 and 3.

To evaluate the designed GCs further, the imaging profiles of the reconstructed PSF can quantitatively reflect its mainlobe and sidelobe performance. In this article, the imaging profiles in different directions, such as the maximum resolution direction ϕ_{\max} , minimum resolution direction ϕ_{\min} , range direction

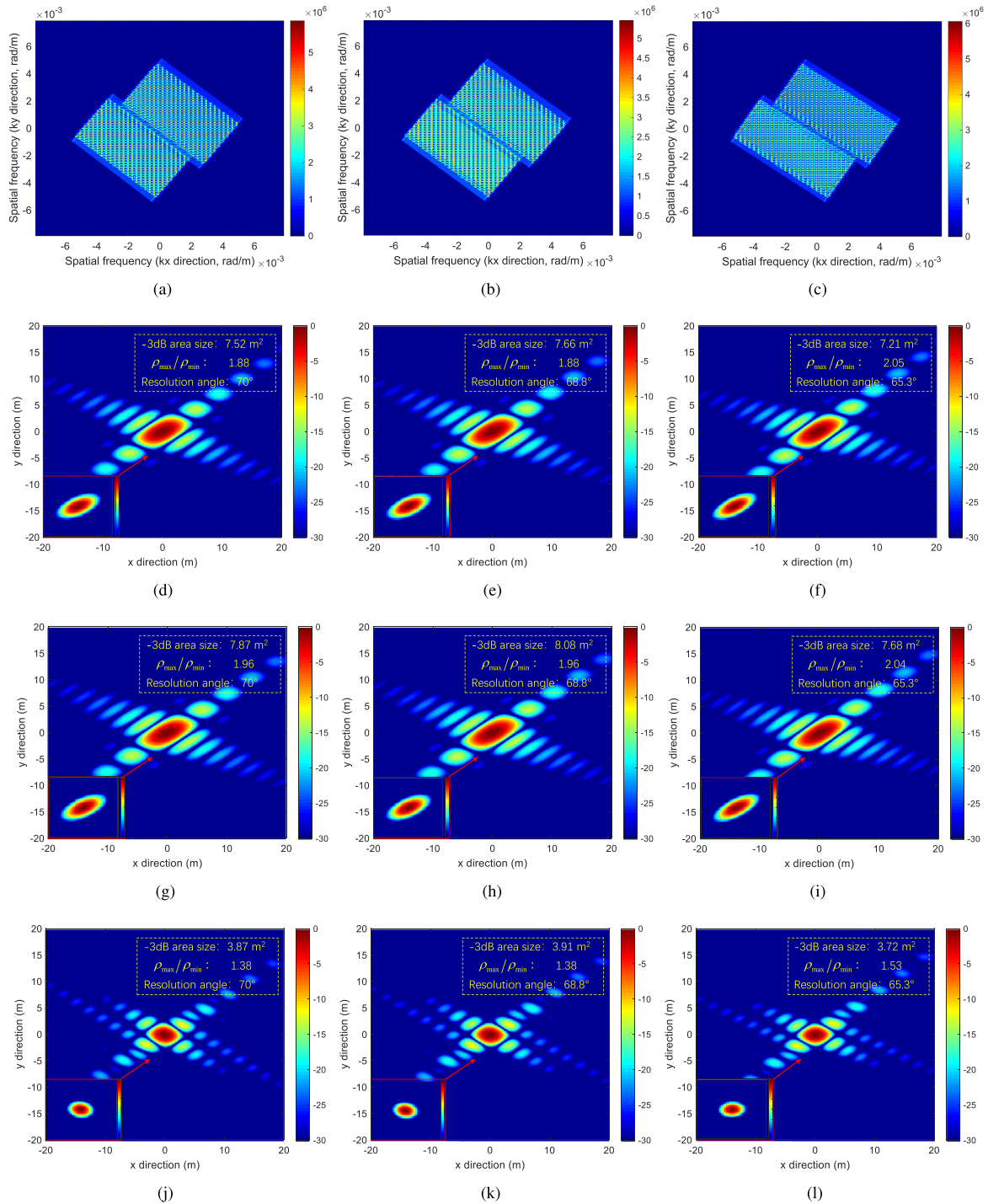


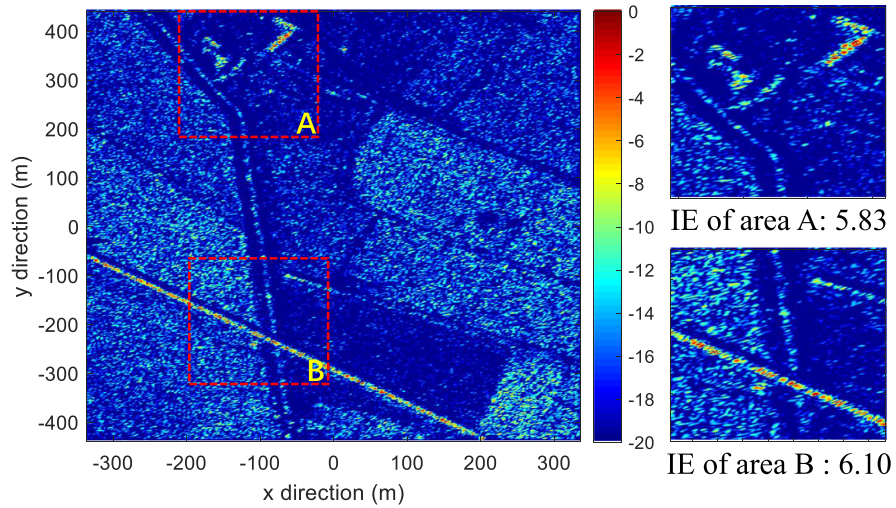
Fig. 8. Imaging results of the point target using the designed GCs. (a)–(c) WSRs of different GCs. (d)–(f) Imaging results of receiver 1. (g)–(i) Imaging results of receiver 2. (j)–(l) Fused imaging results of different GCs.

ϕ_{range} , and cross-range direction ϕ_{cross} , are evaluated by their PSLRs and ISLRs, which are shown in Table III.

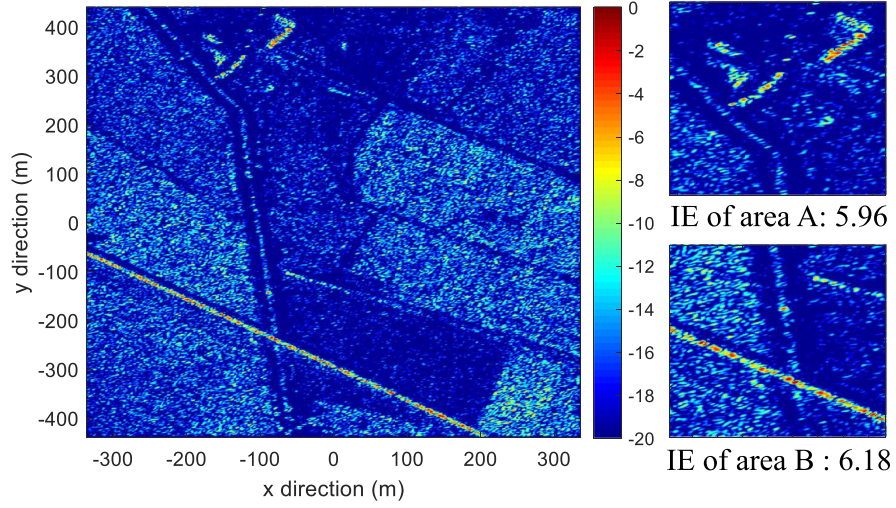
From Table III, the PSLRs and ISLRs of the PSFs of the designed GCs are similar. However, the third GC is slightly better than the other two GCs. Moreover, the third GC can obtain the highest spatial resolution. The following simulations are carried out based on the third GC, and they operate on a GPU platform, Nvidia MX350. The results are shown by MATLAB R2018a.

2) *Distributed Targets With Two Receivers*: Based on the system parameters in Table I and the third GC, the simulated results are shown in Fig. 9 to verify the optimized GC for distributed targets. The echo phase errors are compensated by wavefront curvature correction [52].

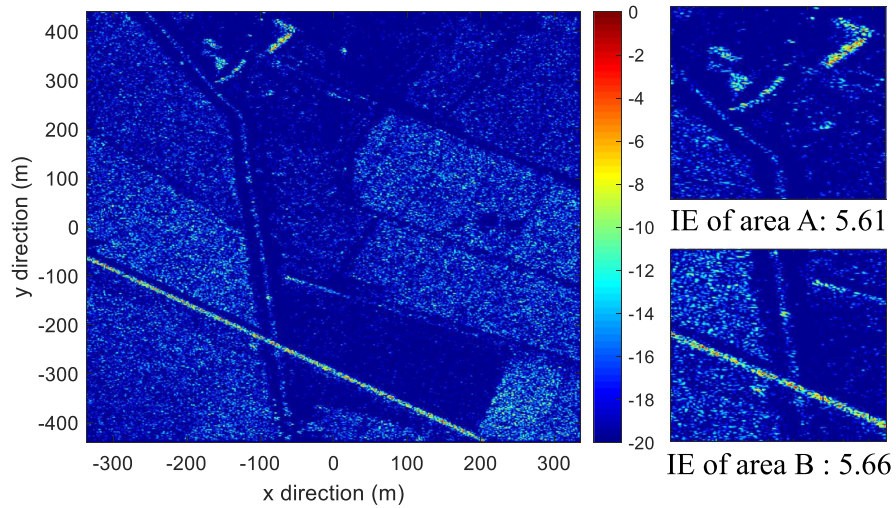
In Fig. 9(a), the strong targets in area A are buildings. The polyline from top to bottom is a road. The strong line from left to right in area B is a rail. The other distributed blocks are



(a)



(b)



(c)

Fig. 9. Imaging results of distributed ground targets using the designed GC 3. (a) Imaging result of receiver 1. (b) Imaging result of receiver 2. (c) Fused imaging result.

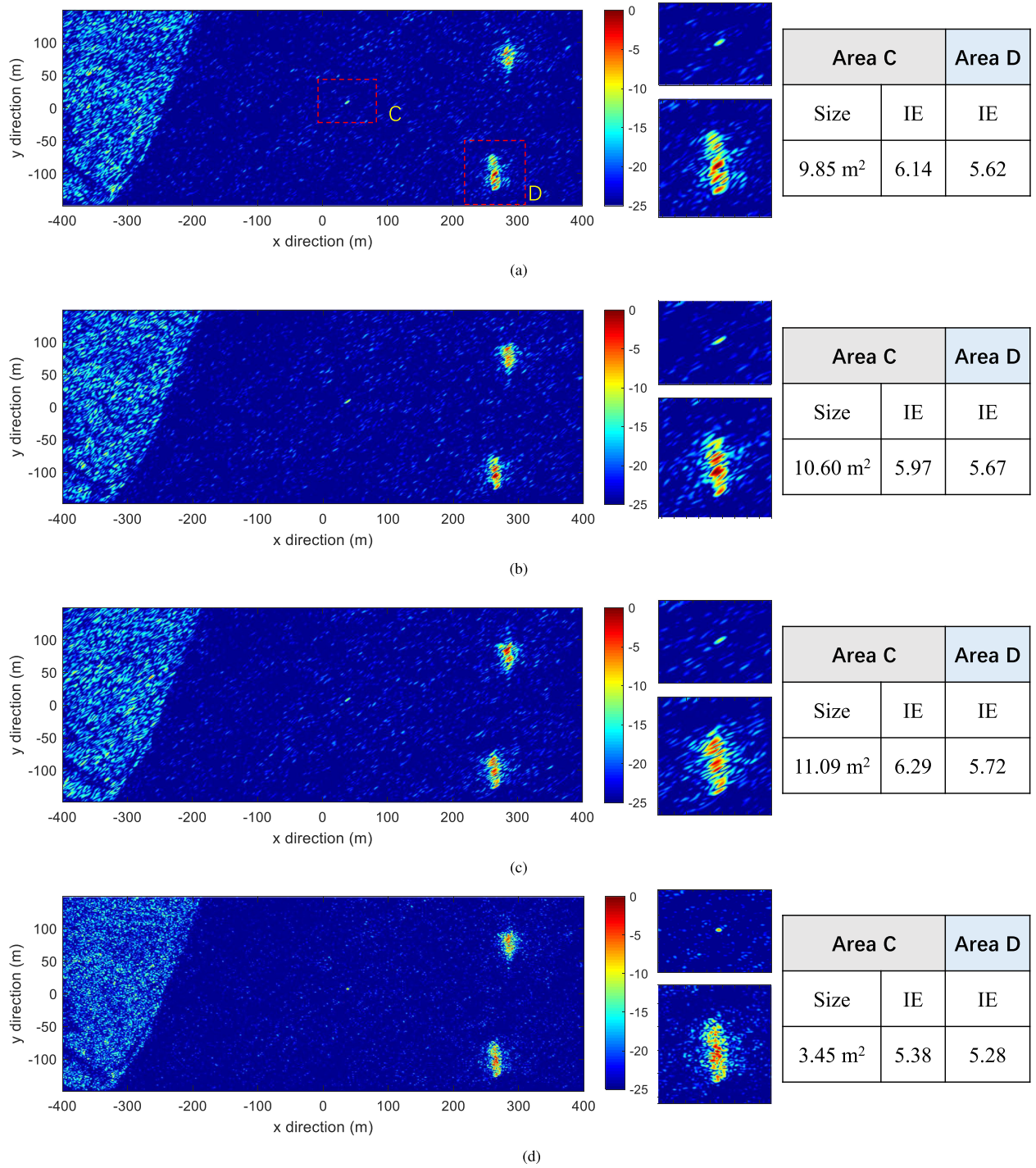


Fig. 10. Imaging results of distributed sea-surface targets using the designed GC 3. (a) Imaging result of receiver 1. (b) Imaging result of receiver 2. (c) Imaging result of receiver 3. (d) Fused imaging result.

farmland. In Fig. 9(a) and (b), the values of the image entropy (IE) of areas A and B are higher than those in the fused image. Besides, the ground clutter of the single receiver is strong. In Fig. 9(c), the clutter is suppressed. Based on the fused image, the resolution of the buildings in area A is improved. In area B, the boundary between the rail and the ground becomes clear.

3) *Distributed Targets With Three Receivers*: When the SA-MuSAR system consists of three receivers, the solution of the CMOP for the two receivers as above can be applied to

simplify the optimization problem. First, the GC vector can be transformed into

$$\vec{g}' = (\Delta\theta_0, \frac{\vec{u}}{|\vec{u}|} * \Delta L, T_a)^T \quad (35)$$

where $\Delta\theta_0$ is the solved flight direction of the leading receiver. The baseline direction of the multiple receivers can be expressed as $\vec{u} = (\Delta x, \Delta z)$, and ΔL denotes the length of the baseline. Based on the solution of the CMOP for the two receivers as

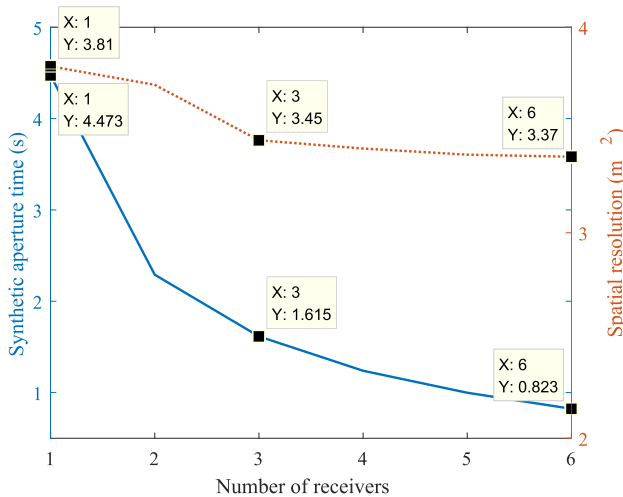


Fig. 11. Relationship between the optimized synthetic aperture time and spatial resolution of SA-MuSAR with different receivers.

above, the GC vector can be simplified by optimizing fewer variables, e.g., ΔL and T_a .

The GC for three receivers can be designed by solving the simplified CMOP. We select the solution with the highest spatial resolution to verify its performance. Based on the system parameters in Table I and the optimized GC parameters, $\Delta L = 532.689$ m and $T_a = 1.615$ s, the simulated results of the SA-MuSAR are shown in Fig. 10.

In Fig. 10, the left part is land, and the right part is two ships on the sea. In area C, the area size of the strong point is large in each bistatic pair, as shown in Fig. 10(a)–(c). Based on the designed GC, the area size of the fused point is nearly one-third that of each individual SA-BiFSAR, as shown in Fig. 10(d). The IEs of area C and area D are reduced in the fused image. Based on the designed GC in this article, SA-MuSAR can coherently fuse echo measurements to obtain a high-resolution radar image.

C. SA-MuSAR With Multiple Receivers

With an increase in the number of receivers, the coherent fusion of SA-MuSAR data becomes a challenge to obtain a high-quality radar imagery [53]. However, it is still necessary to design the appropriate GC, which is a basic requirement for the fusion of SA-MuSAR. The relationship between the optimized synthetic aperture time and spatial resolution of SA-MuSAR with different receivers is shown in Fig. 11.

It is seen that the optimized spatial resolution sizes of the SA-MuSAR with different receivers are similar. However, the synthetic aperture time decreases as the number of receivers increases. The synthetic aperture time can be reduced to less than 1 s using five receivers. Compared with traditional SA-BiFSAR, SA-MuSAR can obtain a high spatial resolution with a short observation time.

VI. CONCLUSION

In this article, a forward-looking GC optimization design method for SA-MuSAR is proposed to obtain a high-quality

image with limited observation time by coherently fusing the measurements of multiple receivers. First, the wavenumber spectrum distribution of SA-MuSAR is adopted to clearly evaluate the relationship between the spatial resolution and the GC. Second, the forward-looking GC optimization problem can be transformed into a CMOP. The optimized spatial resolution of SA-MuSAR can be obtained by straightforwardly constraining the characteristics of the wavenumber spectrum distribution. Based on the designed forward-looking GC, the SA-MuSAR system can efficiently obtain a focused, balanced, and regular PSF. As the number of receivers increases, SA-MuSAR can obtain a high forward-looking spatial resolution with a shorter observation time.

ACKNOWLEDGMENT

The authors would like to thank anonymous reviewers sincerely for their constructive criticisms that improve this article significantly.

REFERENCES

- [1] M. D&'Errico, *Distributed Space Missions for Earth System Monitoring*. Berlin, Germany: Springer Science and Business Media, 2012, vol. 31.
- [2] D. Bruno, S. E. Hobbs, and G. Ottavianelli, "Geosynchronous synthetic aperture radar: Concept design, properties and possible applications," *Acta Astronaut.*, vol. 59, no. 1–5, pp. 149–156, 2006.
- [3] U. Nithirochanant, M. Antoniou, and M. Cherniakov, "Passive coherent multistatic SAR using spaceborne illuminators," *IET Radar, Sonar Navig.*, vol. 14, no. 4, pp. 628–636, 2020.
- [4] Y. Zhang *et al.*, "Fast inverse-scattering reconstruction for airborne high-squint radar imagery based on doppler centroid compensation," *IEEE Trans. Geosci. Remote Sens.*, 2021, doi:10.1109/TGRS.2021.3069499.
- [5] V. Krishnan, J. Swoboda, C. E. Yarman, and B. Yazici, "Multistatic synthetic aperture radar image formation," *IEEE Trans. Image Process.*, vol. 19, no. 5, pp. 1290–1306, May 2010.
- [6] Y. Li, A. Monti Guarnieri, C. Hu, and F. Rocca, "Performance and requirements of GEO SAR systems in the presence of radio frequency interferences," *Remote Sens.*, vol. 10, no. 1, 2018, Art. no 82.
- [7] C. Hu, Y. Li, X. Dong, and D. Ao, "Avoiding the ionospheric scintillation interference on geosynchronous SAR by orbit optimization," *IEEE Geosci. Remote Sens. Lett.*, vol. 13, no. 11, pp. 1676–1680, Nov. 2016.
- [8] Z. Meng, Y. Li, C. Li, M. Xing, and Z. Bao, "A raw data simulator for bistatic forward-looking high-speed maneuvering-platform SAR," *Signal Process.*, vol. 117, pp. 151–164, 2015.
- [9] Z. Sun, J. Wu, J. Pei, Z. Li, Y. Huang, and J. Yang, "Inclined geosynchronous spaceborne-airborne bistatic SAR: Performance analysis and mission design," *IEEE Trans. Geosci. Remote Sens.*, vol. 54, no. 1, pp. 343–357, Jan. 2016.
- [10] H. An, J. Wu, Z. Sun, J. Yang, Y. Huang, and H. Yang, "Topology design for geosynchronous spaceborne-airborne multistatic SAR," *IEEE Geosci. Remote Sens. Lett.*, vol. 15, no. 11, pp. 1715–1719, Nov. 2018.
- [11] D. Massonnet, "The interferometric cartwheel: A constellation of passive satellites to produce radar images to be coherently combined," *Int. J. Remote Sens.*, vol. 22, no. 12, pp. 2413–2430, 2001.
- [12] H. M. Braun and S. Kicherer, "External calibration for CRS-1 and SAR-Lupe," in *Proc. EUSAR*, 2006. [Online]. Available: <https://www.vde-verlag.de/proceedings-de/562960086.html>
- [13] D. Massonnet, "Capabilities and limitations of the interferometric cartwheel," *IEEE Trans. Geosci. Remote Sens.*, vol. 39, no. 3, pp. 506–520, Mar. 2001.
- [14] W. Dower and M. Yearly, "Bistatic SAR: Forecasting spatial resolution," *IEEE Trans. Aerosp. Electron. Syst.*, vol. 55, no. 4, pp. 1584–1595, Aug. 2019.
- [15] T. Tsao, M. Slamani, P. Varshney, D. Weiner, H. Schwarzlander, and S. Borek, "Ambiguity function for a bistatic radar," *IEEE Trans. Aerosp. Electron. Syst.*, vol. 33, no. 3, pp. 1041–1051, Jul. 1997.
- [16] R. Sedwick, T. Hacker, and D. Miller, "Optimum aperture placement for a space-based radar system using separated spacecraft interferometry," in *Proc. Guidance, Navig., Control Conf. Exhibit*, 1999, paper no. 4271.

- [17] A. Das and R. Cobb, "Techsat 21-Space Missions Using Collaborating Constellations of Satellites," 1998.
- [18] H. Fiedler, G. Krieger, F. Jochim, M. Kirschner, and A. Moreira, "Analysis of Bistatic Configurations for Spaceborne SAR Interferometry," in *Proc. EUSAR2002*, pp. 29–32.
- [19] J. NAsA, "Global earthquake satellite system: A 20-year plan to enable earthquake prediction," Technology Report JPL, pp. 400–1069, 2003.
- [20] S. Hobbs, *GeoSAR: Summary of the Group Design Project MSc in Astronautics and Space Engineering*. Cranfield, England: Cranfield University, 2006.
- [21] F. Santi, M. Bucciarelli, D. Pastina, M. Antoniou, and M. Cherniakov, "Spatial resolution improvement in GNSS-based SAR using multistatic acquisitions and feature extraction," *IEEE Trans. Geosci. Remote Sens.*, vol. 54, no. 10, pp. 6217–6231, Oct. 2016.
- [22] F. Liu, X. Fan, L. Zhang, T. Zhang, and Q. Liu, "GNSS-based SAR for urban area imaging: Topology optimization and experimental confirmation," *Int. J. Remote Sens.*, vol. 40, no. 12, pp. 4668–4682, 2019.
- [23] Z. Li, S. Papson, and R. M. Narayanan, "Data-level fusion of multilook inverse synthetic aperture radar images," *IEEE Trans. Geosci. Remote Sens.*, vol. 46, no. 5, pp. 1394–1406, May 2008.
- [24] P. K. Rennich, M. D. Casciato, A. M. Chan, and S. D. Eye, "Coherent multistatic SAR collections and target phenomenology," in *Proc. Eur. Radar Conf.*, 2008, pp. 152–155.
- [25] F. Santi, M. Antoniou, and D. Pastina, "Point spread function analysis for GNSS-based multistatic SAR," *IEEE Geosci. Remote Sens. Lett.*, vol. 12, no. 2, pp. 304–308, Feb. 2015.
- [26] F. Daout, F. Schmitt, G. Ginolhac, and P. Fargette, "Multistatic and multiple frequency imaging resolution analysis-application to GPS-based multistatic radar," *IEEE Trans. Aerosp. Electron. Syst.*, vol. 48, no. 4, pp. 3042–3057, Oct. 2012.
- [27] T. Derham, S. Doughty, C. Baker, and K. Woodbridge, "Ambiguity functions for spatially coherent and incoherent multistatic radar," *IEEE Trans. Aerosp. Electron. Syst.*, vol. 46, no. 1, pp. 230–245, Jan. 2010.
- [28] I. Bradaric, G. Capraro, D. Weiner, and M. Wicks, "Multistatic radar systems signal processing," in *Proc. IEEE Conf. Radar*, 2006, paper no. 8.
- [29] U. Nithirochanant, M. Antoniou, and M. Cherniakov, "Passive coherent multistatic SAR: Experimental results with a point-like target," in *Proc. 20th Int. Radar Symp.*, 2019, pp. 1–6.
- [30] L. Zhang, H.-l. Li, Z.-j. Qiao, and Z.-w. Xu, "A fast BP algorithm with wavenumber spectrum fusion for high-resolution spotlight SAR imaging," *IEEE Geosci. Remote Sens. Lett.*, vol. 11, no. 9, pp. 1460–1464, Sep. 2014.
- [31] N. Sakar, M. Rodriguez-Cassola, P. Prats-Iraola, and A. Moreira, "Doppler based azimuth reconstruction algorithm for multistatic SAR formations in high resolution wide swath mode," in *Proc. IEEE Int. Geosci. Remote Sens. Symp.*, 2019, pp. 1124–1127.
- [32] N. Sakar, M. Rodriguez-Cassola, P. Prats-Iraola, and A. Moreira, "Azimuth reconstruction algorithm for multistatic SAR formations with large along-track baselines," *IEEE Trans. Geosci. Remote Sens.*, vol. 58, no. 3, pp. 1931–1940, Mar. 2020.
- [33] Z. Ding, W. Gao, J. Liu, T. Zeng, and T. Long, "A novel range grating lobe suppression method based on the stepped-frequency SAR image," *IEEE Geosci. Remote Sens. Lett.*, vol. 12, no. 3, pp. 606–610, Mar. 2015.
- [34] Z. Ding, Y. Guo, W. Gao, Q. Kang, T. Zeng, and T. Long, "A range grating lobes suppression method for stepped-frequency SAR imagery," *IEEE J. Sel. Topics Appl. Earth Observ. Remote Sens.*, vol. 9, no. 12, pp. 5677–5687, Dec. 2016.
- [35] C. Hu, Z. Chen, X. Dong, and C. Cui, "Multistatic geosynchronous SAR resolution analysis and grating lobe suppression based on array spatial ambiguity function," *IEEE Trans. Geosci. Remote Sens.*, vol. 58, no. 9, pp. 6020–6038, Sep. 2020.
- [36] R. Wang *et al.*, "Processing the azimuth-variant bistatic SAR data by using monostatic imaging algorithms based on two-dimensional principle of stationary phase," *IEEE Trans. Geosci. Remote Sens.*, vol. 49, no. 10, pp. 3504–3520, Oct. 2011.
- [37] T. Zeng, M. Cherniakov, and T. Long, "Generalized approach to resolution analysis in BSAR," *IEEE Trans. Aerosp. Electron. Syst.*, vol. 41, no. 2, pp. 461–474, Apr. 2005.
- [38] G. Garza and Z. Qiao, "Resolution analysis of bistatic SAR," in *Radar Sensor Technol. XV*, vol. 8021. International Society for Optics and Photonics, 2011, paper no. 80211V.
- [39] M. I. Duersch, "Backprojection for Synthetic Aperture Radar," Brigham Young University, Provo, Utah, 2013. [Online]. Available: <https://scholarsarchive.byu.edu/cgi/viewcontent.cgi?article=5059&context=etd>
- [40] M. Cherniakov, "Space-surface bistatic synthetic aperture radar-prospective and problems," pp. 22–25, 2002. [Online]. Available: <http://www.geo.uzh.ch/microsite/rs-l-documents/research/SARlab/BistaticLiterature/Ver09/PDF/Che02.pdf>
- [41] C. E. Yarman, B. Yazici, and M. Cheney, "Bistatic synthetic aperture radar imaging for arbitrary flight trajectories," *IEEE Trans. Image Process.*, vol. 17, no. 1, pp. 84–93, Jan. 2008.
- [42] S. Wang, V. M. Patel, and A. Petropulu, "Multidimensional sparse fourier transform based on the fourier projection-slice theorem," *IEEE Trans. Signal Process.*, vol. 67, no. 1, pp. 54–69, Jan. 2019.
- [43] R. J. Mailloux, *Phased Array Antenna Handbook*. Norwood, MA, USA: Artech House, 2017.
- [44] L. D. Stone, *Theory of Optimal Search*. New York, NY, USA: Elsevier, 1976.
- [45] J. Zheng, T. Su, W. Zhu, and Q. H. Liu, "A fast non-searching algorithm for the high-speed target detection," in *Prog. Syst. Eng.* New York, NY, USA: Springer, 2015, pp. 777–782.
- [46] R. Bracewell, K.-Y. Chang, A. Jha, and Y.-H. Wang, "Affine theorem for two-dimensional fourier transform," *Electron. Lett.*, vol. 29, no. 3, pp. 304–304, 1993.
- [47] K. Deb, A. Pratap, S. Agarwal, and T. Meyarivan, "A fast and elitist multiobjective genetic algorithm: NSGA-II," *IEEE Trans. Evol. Comput.*, vol. 6, no. 2, pp. 182–197, Apr. 2002.
- [48] J. Pei, Y. Huang, Z. Sun, Y. Zhang, J. Yang, and T.-S. Yeo, "Multiview synthetic aperture radar automatic target recognition optimization: Modeling and implementation," *IEEE Trans. Geosci. Remote Sens.*, vol. 56, no. 11, pp. 6425–6439, Nov. 2018.
- [49] S. Mirjalili, "Genetic Algorithm," in *Evol. Algorithms Neural Netw.* Springer, 2019, pp. 43–55.
- [50] C. M. Fonseca, P. J. Fleming *et al.*, "Genetic algorithms for multiobjective optimization: Formulation discussion and generalization," in *ICGA*, vol. 93, 1993, pp. 416–423.
- [51] A. Konak, D. W. Coit, and A. E. Smith, "Multi-objective optimization using genetic algorithms: A tutorial," *Rel. Eng. Syst. Saf.*, vol. 91, no. 9, pp. 992–1007, 2006.
- [52] Y. Miao, J. Wu, Z. Li, and J. Yang, "A generalized wavefront-curvature-corrected polar format algorithm to focus bistatic SAR under complicated flight paths," *IEEE J. Sel. Topics Appl. Earth Observ. Remote Sens.*, vol. 13, pp. 3757–3771, 2020, doi: [10.1109/JSTARS.2020.2999966](https://doi.org/10.1109/JSTARS.2020.2999966).
- [53] G. Krieger and M. Younis, "Impact of oscillator noise in bistatic and multistatic SAR," *IEEE Geosci. Remote Sens. Lett.*, vol. 3, no. 3, pp. 424–428, Jul. 2006.



Deqing Mao (Student Member, IEEE) received the B.S. degree from the School of Electronic Engineering, Chengdu University of Information Technology, Chengdu, China, in 2014. He is currently working toward the Ph.D. degree with the School of Information and Communication Engineering, University of Electronic Science and Technology of China, Chengdu, China.

His research interests include radar signal processing, multistatic radar, and inverse problem in radar imaging.



Yongchao Zhang (Member, IEEE) received the B.S. degree in electronic information engineering from Hainan University, Haikou, China, in 2011, and the Ph.D. degree from the School of Information and Communication Engineering, University of Electronic Science and Technology of China (UESTC), Chengdu, China, in 2018.

From 2016 to 2017, he was a Visiting Student with the Lund University, Lund, Sweden. He is currently an Associate Research Fellow with the School of Information and Communication Engineering, UESTC.

His research interests include array signal processing and inverse problem in radar applications.



Jifang Pei (Member, IEEE) received the B.S. degree from the College of Information Engineering, Xiangan University, Hunan, China, in 2010, the M.S. degree from the School of Electronic Engineering, University of Electronic Science and Technology of China (UESTC), Chengdu, China, in 2013, and the Ph.D. degree from the School of Information and Communication Engineering, UESTC, Chengdu, China, in 2018.

From 2016 to 2017, he was a Joint Ph.D. Student with the Department of Electrical and Computer Engineering, National University of Singapore, Singapore. He is currently an Associate Research Fellow with the School of Information and Communication Engineering, UESTC. His research interests include radar target recognition, radar signal processing and machine learning.



Yulin Huang Senior Member, IEEE) received the B.S. and Ph.D. degrees in electronic engineering from the University of Electronic Science and Technology of China (UESTC), Chengdu, China, in 2002, and 2008, respectively.

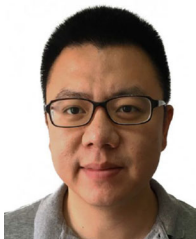
From 2013 to 2014, he was a Visiting Researcher with the University of Houston, Houston, TX, USA. Since 2016, he has been a Professor with the School of Information and Communication Engineering, UESTC. He has authored more than 100 journal and conference papers. His research interests include synthetic aperture radar, target detection and recognition, artificial intelligence, and machine learning.

Dr. Huang is also a member of the IEEE Aerospace and Electronic Systems Society.



Weibo Huo (Member, IEEE) received the B.S. degree from the School of Science, Shandong Jianzhu University, Jinan, China, in 2010, and the Ph.D. degree from the School of Information and Communication Engineering, University of Electronic Science and Technology of China, Chengdu, China, in 2019.

His research interests include radar signal processing, radar target detection and sea clutter modeling and simulation.



Yin Zhang (Member, IEEE) received the B.S. and Ph.D. degrees in electronic information engineering from University of Electronic Science and Technology of China (UESTC), Chengdu, China, in 2008 and 2016, respectively.

From 2015 to 2016, he was a Visiting Student with the University of Delaware, Newark, DE, USA. He is currently an Associate Research Fellow with the School of Information and Communication Engineering, UESTC. His research interests include radar imaging and signal processing in related radar

applications.



Jianyu Yang Member, IEEE) received the B.S. degree from the National University of Defense Technology, Changsha, China, in 1984, and the M.S. and Ph.D. degrees from the University of Electronic Science and Technology of China (UESTC), Chengdu, in 1987 and 1991, respectively.

In 2005, he visited Massachusetts Institute of Technology, USA. Since 1999, he has been a Professor with the School of Information and Communication Engineering, UESTC. He has authored more than 150 journal and conference papers. His research interests

are mainly in synthetic aperture radar and statistical signal processing

Dr. Yang is a fellow of the Chinese Institute of Electronics.